Contents lists available at ScienceDirect

Materials Today Communications

Ab initio investigations of the interfacial bond of Fe(001)/Al(001)

Soon-Dong Park [a], Sung Youb Kim [b], Daeyong Kim [a],*

[a] *Materials Deformation Department, Korea Institute of Materials Science, Changwon, 51508, Republic of Korea*
[b] *School of Mechanical, Aerospace and Nuclear Engineering, Ulsan National Institute of Science and Technology, Ulsan 44919, Republic of Korea*

A B S T R A C T

Density functional theory-based *ab initio* simulations were performed to investigate the bond strength of an Fe (001)/Al(001) coherent interface, its atomic configuration, oxidation at the interface, and mechanical deformation along the lateral direction of the interface. The bcc-type interface exhibited the highest bond strength in terms of the work of separation, but the bond strength decreased significantly when oxygen was introduced. The fracture of the bare interface initiated at the Al matrix under tensile loading, whereas that of the oxidized interface began at the interface because oxygen deteriorated the high bond strength between the Fe and Al atoms. Additionally, the bond strength of the interface was investigated under different biaxial strains to understand the effect of the residual stress generated during the joining process of Fe(001)/Al(001). Based on our findings, the mechanical deformation along the lateral direction does not significantly impact the bond strength.

1. Introduction

Joining technologies have attracted significant interest in numerous industries such as automotive [1–4], medical [5,6], and aerospace [7,8] due to the functional advantages of chemically and physically connected dissimilar materials. The development of numerous technologies has resulted in the successful joining of various metals, including aluminum/steel [2–4], aluminum/titanium [9,10], and copper/steel [11]. Particularly, the combination of steel and aluminum has been extensively employed in the manufacturing of car body parts to lower the weight of the product without reducing the strength, resulting in an enhanced fuel consumption efficiency and reduced CO_2 gas emission. These metal joining processes are commonly divided into two groups: fusion welding and solid-state welding. The former induces phase transformation at the interface by the thermal heat around the melting temperature based on electrical (arc, laser beam, resistance welding) or chemical (gas, exothermic welding) sources. Solid-state welding achieves coalescence between two dissimilar metals by external loading without melting such as cold, roll, electromagnetic welding. During fusion welding, the intermetallic compound (IMC) phase was generated after solidification due to the difference in thermal properties between the two dissimilar materials [12]. Furthermore, micro-cracks formed readily and the propagation of the fracture initiated in the IMC layer [13], in which the interface was brittle and weak, deteriorating the mechanical properties of the welded material. However, the mechanical

and chemical properties of bonded interfaces obtained via solid-state welding can be better than those obtained via fusion welding. This is because the formation of the IMC layer and heat-affected zone (HAZ) is relatively minimized owing to the low temperature of the metals being welded and the experimental condition of joining [14–16]. Consequently, electromagnetic forming (EMF) [17–19], a solid-state welding technology, has emerged as a novel alternative to fusion welding. Electromagnetic welding can be used in mass production once the electrical parameters for the experimental conditions have been established [20].

EMF, also referred to as impulse forming, is a high-speed forming technology that utilizes the Lorentz force generated by interactions between the magnetic field by instantaneous discharge with high energy and eddy currents generated from the magnetic field. In the EMF process, plastic deformation at the material interface due to high-speed impulse causes the material interface to behave like a high-viscosity fluid, eventually forming a wavy interface [21]. Additionally, under specific conditions such as a suitable collision velocity and angle of collision, the jetting effect occurs on the surface, thereby efficiently removing the oxide layer and impurities, forming a clean surface between two metals [22,23]. These phenomena have been proposed to comprehensively explain the strong bond between two dissimilar materials after the EMF process. To further comprehend the EMF process, various simulations with different computational schemes have been conducted. Using smoothed particle hydrodynamics (SPH), Nassiri et al.

demonstrated the occurrence of a wavy morphology and jetting phenomena at the interface during high-speed impulse [24]. Moreover, atomic simulations, such as molecular dynamics, have been utilized for predicting the properties of the interface [25,26]. Chen et al. demonstrated that atomic diffusion mainly occurred at a specific stage, namely the unloading stage. Further, the higher diffusion coefficient resulted in the generation of a diffusion layer [25]. Additionally, using density functional theory (DFT) calculations, the properties of the Fe/Al interface were calculated to investigate the work of separation (WS) and the role of oxidation at the interface [27,28]. However, there are limited studies on the bond strength and the associated factors for modulating the bond strength during the EMF process for welding Fe/Al bimetallic systems.

In this study, we utilized first-principles DFT calculations to determine whether the conditions during the EMF process could control the bond strength of the Fe/Al coherent interface, which is characterized by the WS (in eV/Å^2) and the mechanical response under tensile loading along the thickness direction. Therefore, we examined the stacking sequence of welding metals, oxidation at the interface, and mechanical deformation along the lateral direction of the interface.

2. Computational method

2.1. First-principles calculations

We performed DFT calculations on the total energy of pure Al, Fe slabs, and the Fe/Al interface structure. All calculations were performed using the Vienna Ab Initio Simulation Package (VASP) based on the spin-polarized density functional theory [29,30]. We used the projector augmented wave (PAW) [31] pseudopotential and generalized gradient approximation (GGA) parameterized by Perdew-Burke-Ernzerhof (PBE) [32]. All the calculations including Fe atoms consider the ferromagnetic characteristics of Fe atoms. The electrons of the wavefunctions achieved a cutoff energy of 500 eV in a plane-wave basis set. The atomic configuration of the ideal bulk was fully relaxed until the forces on the ions became < 0.01 eVÅ^{-1} with 10^{-8} eV/cell of the energy convergence. The slab or interface structures were fully relaxed in the direction normal to the surface or interface. The (001) surfaces of Fe and Al, which are low-index surfaces, were selected to create a coherent interface. The Monkhorst-Pack grid [33] was $25 \times 25 \times 25$ k points for the optimization of the bulk structure and $25 \times 25 \times 1$ k points for the relaxation of the slab and interface structure. Herein, the x-, y-, and z-directions were assigned to the [001], [010], and [001] directions, respectively. The slab structures were modeled by applying a vacuum along the [001] direction at ~20 Å to the bulk structure, as shown in Fig. 1(a). Further, periodic conditions were applied along the in-plane directions (i.e., the [110] and [1$\bar{1}$0] directions).

2.2. Tensile test

As described in Section 3.2, we utilized the rigid grain shift method (RGS) [34–36]. Particularly, a vacuum layer was gradually added to the optimized interface configuration between the Fe and Al atoms along the perpendicular direction ([001]-direction), which corresponds to the insertion of a pre-crack at the interface. Self-consistence calculations were performed, indicating that atomic relaxations were not allowed.

In the Sections 3.3 and 3.4, the mechanical strain was homogeneously applied to the entire Fe(001)/Al(001) structure, i.e. the so-called homogeneous lattice extension (HLE) [37,38] to determine which layer broke first. Particularly, the two outermost layers of Fe(001) and Al(001) from the interface were fixed, while under the constraints of the lattice, the atomic configurations of the other layers were relaxed to assess tensile loading.
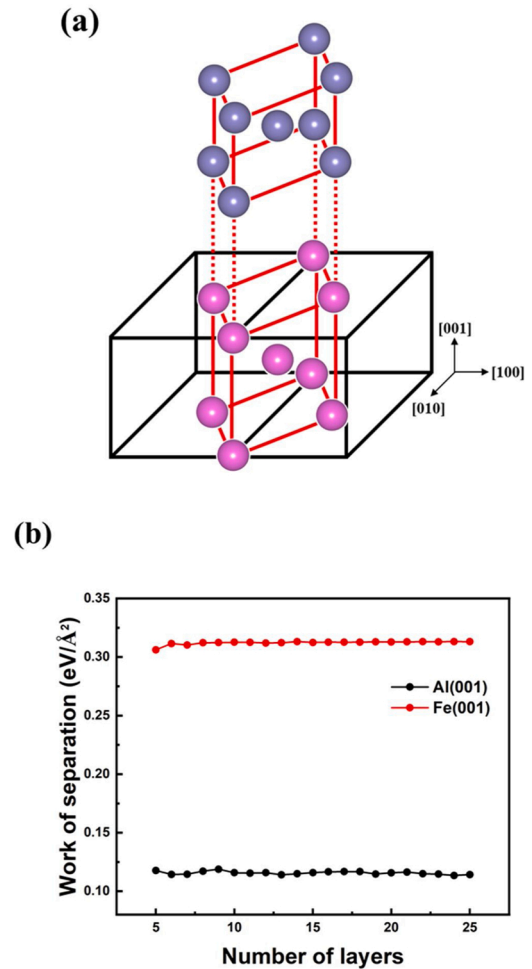

Fig. 1. (a) Schematic illustration of the bcc Fe (upper) and bct Al (lower) structures. The bct configuration highlighted by the red line is modeled from two adjacent fcc unit cells denoted by the black line. The violet and magenta spheres correspond to the Fe and Al atoms, respectively. (b) WS of the bare Fe (001) and Al(001) slabs with different thicknesses.

3. Results and discussion

3.1. Bulk structure

The reliability of our calculation conditions was confirmed by first calculating bulk properties such as the lattice parameters and elastic constants of ideal body-centered cubic (bcc) Fe and face-centered cubic (fcc) Al. The bulk structures of Fe and Al were completely optimized to obtain an equilibrium state with lattice constants of 2.831 Å and 4.040 Å, respectively. The estimated results summarized in Table 1 are in good agreement with the results of the previous DFT and experimental reports

Table 1

Lattice parameter (a), elastic constants (C_{11}, C_{12}, C_{14}), and work of separation (W_{sep} along the [001] direction) of bcc Fe and fcc Al. The experimental lattice parameter, elastic constants of bcc Fe and fcc Al at 4 K were obtained from [41] and [45], respectively.

System	a (Å)	C_{11} (GPa)	C_{12} (GPa)	C_{44} (GPa)	W_{sep} (eV/Å^2)
	2.831	274.296	145.002	93.085	0.312
bcc Fe	2.830 [39]	286 [39]	147 [39]	99 [39]	0.304 [40]
	2.860 [41]	245 [41]	139 [41]	122 [41]	0.301 [42]
	4.040	109.114	62.788	28.437	0.116
fcc Al	4.06 [43]	117.5 [44]	63.5 [44]	35.5 [44]	0.107 [43]
	4.02 [45]	114.3 [45]	61.9 [45]	31.6 [45]	0.143 [42]

[39–45]. Therefore, we believe that our computational parameters are appropriate for further investigation of the properties of the Fe(001)/Al (001) coherent interface.

3.2. Interface structure

The coherent interface of Fe(001)/Al(001) was constructed by transforming the Al crystal structure from the fcc (black line) structure to the body-centered tetragonal (bct, red line) structure by rotating the unit vectors, as shown in Fig. 1(a). Thus, the lattice parameter (2.856 Å) along the [110] and [$1\bar{1}0$] directions for the bct Al structure was utilized. Subsequently, a biaxial compression of ~0.88 % was applied to the bct Al configuration along the [110] and [$1\bar{1}0$] directions to eliminate the mismatch between bcc Fe and bct Al. Sufficiently thick Fe(001) and Al(001) slabs, which minimize the surface effect inside the structure, were obtained by investigating the WS as a function of the thickness, as shown in Fig. 1(b). WS refers to the energy required to separate the two free surfaces, which is twice the surface energy (in eV/Å^2). This condition only occurs when both the cleavage surfaces are symmetrically equivalent [46]. The WS for a single element material was obtained using differences in the total energy between the nanoplate and its bulk counterpart per cross-sectional area. Our results showed that the WS for Fe(001) and Al(001) slabs exhibited a consistent tendency with different thicknesses, at ~0.312 and ~0.116 eV/Å^2, respectively, as summarized in Table 1. Numerous computational simulations confirmed that the surface energy of metal slabs became size-independent when more than five layers were employed [47–49]. Once the WS of the Fe(001)/Al(001) interface was known, it was possible to predict the interfacial fracture toughness and energy, which are the parameters required for evaluating the fracture and nucleation resistances [50,51], respectively. These parameters have been discussed in the later sections. Hence, we noted that to assess the robust joining of Fe(001) and Al(001) in terms of interfacial fracture toughness, which was dependent on the WS of the interface, the WS of the interface structure must exceed that of pure Al(001). That is, under external loading, the fracture could initiate at the Al matrix because the WS is lower than that of the Fe/Al interface.

To investigate the bond characteristics of the Fe(001)/Al(001) interface, we considered three types of interface configurations with the bcc (four-coordinate Fe and Al atoms), bridge (two-coordinate), and top (one-coordinate) positions shown in the inset of Fig. 2(a). Fig. 2(a) shows the WS as a function of the thickness. Herein, an equal number of layers for each of the Fe(001) and Al(001) slabs was modeled. The WS at the interface for the two materials combined is defined as:

$$W_{sep} = \frac{E_{Fe(001)} + E_{Al(001)} - E_{Fe(001)/Al(001)}}{A} \quad (1)$$

where $E_{Fe(001)}$ and $E_{Al(001)}$ are the total energies of the Fe(001) and Al (001) nanoplates with free surfaces, respectively. $E_{Fe(001)/Al(001)}$ is the total energy of the Fe(001)/Al(001) interface model, in which the same number of layers is utilized for the Fe(001) and Al(001) slabs; A is the interfacial area. The WS of the interface structure is independent of size as a result of the Fe(001) and Al(001) slabs. Furthermore, by evaluating optimized structure of the bulk-type (Fig. S1 of Supporting Information) interface, we observe that the free surface would not significantly affect the WS of the interface, approximately ~0.253 eV/Å^2. Interestingly, the strong bond between Fe and Al for the bcc and bridge-type interfaces was confirmed by the WS values of 0.252 and 0.145 eV/Å^2, respectively, as shown in Fig. 2(a). However, the WS of the top type was only 0.093 eV/Å^2, which was lower than that of Al(001). Czelej et al. [27] achieved a WS value of ~0.194 eV/Å^2 for the semi-coherent Fe(001)/A(001) interface, which lies in the mid-range of the results obtained for the bcc and bridge interfaces. The atomic distances between Fe and the neighboring Al atoms for the interfaces examined were almost similar (~2.50 Å), as listed in Table 2. Fig. 2(b) shows the planar charge density difference for the bcc, bridge, and top Fe(001)/Al(001) interfaces along the
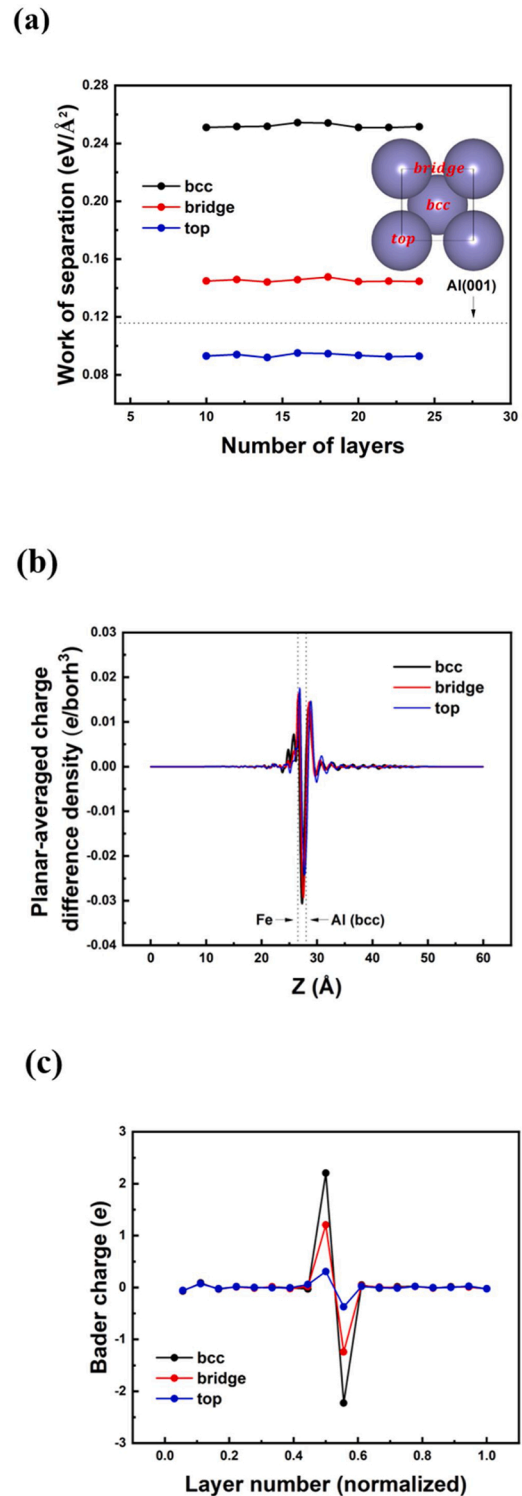
(a)

(b)

(c)

Fig. 2. (a) WS of the bcc, bridge, and top Fe(001)/Al(001) interfaces with different number of layers. The number of layers indicates the total layers in the Fe(001)/Al(001) interface model. The insertion is the top view of the Fe(001) slab with the three possible stacking positions for the Al atom, namely bcc-, bridge-, and top-site. (b) Planar-averaged charge density difference along the [001]-direction. (c) Bader charge as a function of the normalized position for the bcc, bridge, and top interfaces.

Table 2
Fe(001)/Al(001) interface structure with calculated bond length between two adjacent Al and Fe atoms at the interface, and Bader charge with different bond types. Herein, the twenty-layered thick nanoplate is analyzed. As shown in the inset of Fig. 3(a), the Bader charges of the tenth Fe atom and first Al atom (from left to right) were estimated. The Bader charges before and after bonding were extracted from the difference in pure slab (interface structure) and its corresponding bulk.

		bcc	bridge	top
bond length (Å)		2.500	2.501	2.512
Bader charge (*e*)	*Before bonding*	−0.025 (Al)	0.061 (Fe)	
	After bonding	−1.873 (Al)	−1.185 (Al)	−0.346 (Al)
		1.858 (Fe)	1.156 (Fe)	0.288 (Fe)

thickness direction. The planar-averaged density difference was obtained as $\Delta\rho(z) = \rho(z)_{Fe(001)/Al(001)} - \rho(z)_{Fe(001)} - \rho(z)_{Al(001)}$, wherein $\rho(z)_{Fe(001)/Al(001)}$, $\rho(z)_{Fe(001)}$, and $\rho(z)_{Al(001)}$ are the planar-averaged charge density of the Fe/Al interface, Fe slab, and Al slab [52,53], respectively. Note that positive and negative values of $\Delta\rho(z)$ indicate charge accumulation and depletion, respectively. For the considered interfaces, significant charge accumulation and depletion were observed at the interface due to the interaction between Fe and Al atoms. Additionally, we observed that the depletion at the Al-side interface relied on the type of interface, resulting in the amount of interaction at the interface. To further observe the quantitative charge distribution, we calculated the charge transfer based on the Bader analysis [54–56] of the bcc, bridge, and top Fe(001)/Al(001) interfaces, as shown in Fig. 2(c). The Bader charge was obtained from the difference in charge between the ideal bulk (Fe and Al) and Fe(001)/Al(001) of the interfacial structure. Fe atoms adjacent to the Al atoms exhibited positive charges, indicating that the electrons were transferred from Al to Fe. The detailed number of Bader charges is summarized in Table 2. Particularly, the Bader charge was highest for the first Fe atom directly adjacent to the Al layer. The other regions of the interface structure were almost similar to those of the corresponding pure bulk, except for the outermost atom due to the surface effect. This means that interaction between the Fe and Al regions mainly occurs at the interface. Consequently, the number of electrons transferred, which enhances the bond strength between the Fe (001) and Al(001) slabs, decreased in the following order: bcc-, bridge-, and top-type interfaces. Additionally, to intensively investigate the bond characteristics of the Fe(001)/Al(001) interface, the total and partial density of states (DOS) [57,58] were plotted in Fig. 3(a). Notably, the total DOS of bcc interface was significantly contributed by 3*d* orbitals of the Fe atoms, with the case of bcc Fe [59]. However, the 3*s* and 3*p* orbitals of the Al atoms were rarely observed as shown in the insertion of Fig. 3(a). In Fig. 3(b), the partial DOS of the selected Fe atom, which is in the free surface (denoted by the dotted arrow) and bonded with the Al atom (denoted by the solid arrow), is displayed. In the case of down-spin, for the considered Fe(001)/Al(001) interfaces, the trend of the partial DOS was almost similar; however, the partial DOS for up-spin exhibited a dependency on the interface type. We note that the energy shift in the partial DOS was observed owing to the interaction between the Fe and Al atoms, and the bonding type. Particularly, valence levels, which ranged from -5 to -2.5 eV, shift to the nearby Fermi level. This energy shift could be attributed to the 3*s*- and 3*p*-orbitals of the Al atoms as shown in the insertion of Fig. 3(a).

As mentioned previously, we estimated the interfacial fracture toughness of the Fe(001)/Al(001) interface, $K_{IC}^{Int} = \sqrt{4W_{sep}E_{001}}$, where W_{sep} is the WS of Fe(001)/Al(001) and E_{100} is the Young's modulus based on bcc Fe or fcc Al in the [001]-direction [50]. Because the interface structure consists of two types of materials, two different values of interfacial toughness were obtained. For the bcc-, bridge-, and top-type Fe(001/Al(001) interfaces, the interfacial fracture toughness was approximately 1.011–1.676, 0.767–1.271, and 0.614–1.018 MPa·$\sqrt{m}$, respectively. Particularly, the interfacial fracture toughness of
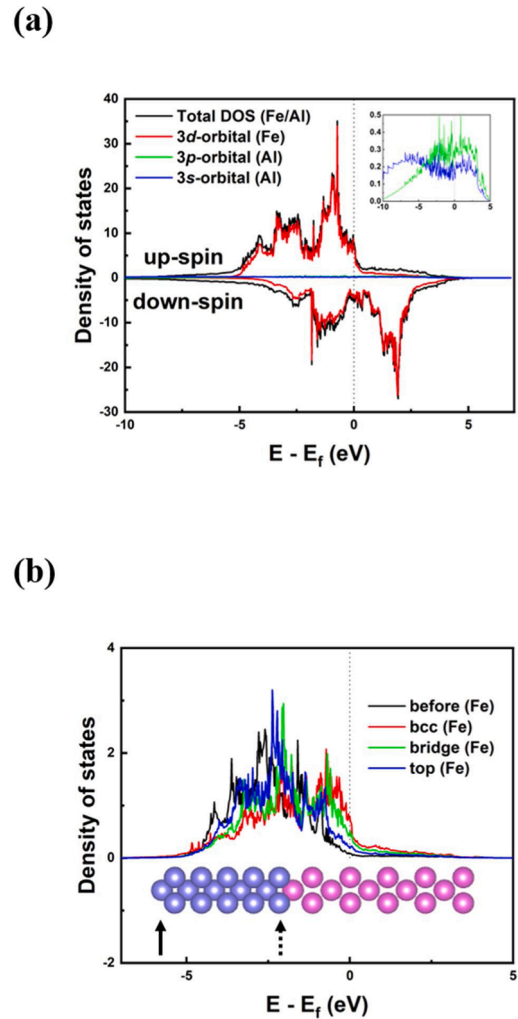

(a)

(b)

Fig. 3. (a) Total and partial DOS for the optimized bcc Fe(001)/Al(001) interface. The insertion shows the DOS corresponding to the Al atoms. The Fermi energy is fitted to 0 eV. (b) Partial DOS of Fe (3*d*-oribitals) atoms *before* and *after* bonding. Partial DOS *before* and *after* bonding of the Fe atoms is denoted by the solid and dotted arrow, respectively.

the bcc and bridge interfaces was higher than that of the Al(001) structure, approximately ~0.686 MPa·$\sqrt{m}$, indicating that the failure can begin at the Al matrix and propagate further as the mechanical deformation increases. Using the DFT scheme, it was observed that the range of the estimated fracture toughness values was similar to that of other metal–metal interfaces [51]. To investigate the thermodynamic stability of the interface configuration, the interfacial energy of Fe (001)/Al(001) was computed: $\gamma_{Int} = \gamma_{surf}^{Fe} + \gamma_{surf}^{Al} - W_{sep}$ where γ_{surf}^{Fe} and γ_{surf}^{Al} are the surface energies of Fe(001) and Al(001) [28,51,60], respectively. The γ_{Int} values of the bcc-, bridge-, and top-type interfaces were –0.038, 0.069, and 0.121 eV/Å^2, respectively. Particularly, the bcc-type Fe(001)/Al(001) interface showed a negative interfacial energy, indicating the possibility of phase transformation to a new phase. This trend for the coherent Fe/Al interface was also predicted by Khalid et al. [28], wherein the interfacial energy was –1.555 eV/ Å^2. The bridge- and top-type interfaces possessed relatively stable configurations because of the weak bonding at these interfaces.

Fig. 4 shows the mechanical properties of the Fe(001)/Al(001) interfaces. The binding energy was obtained by determining the difference in the WS of the interfaces with and without separation. The calculated binding energy was well fitted to the universal binding energy relation (UBER) [61–63], as shown in Fig. 4(a). By differentiating the binding
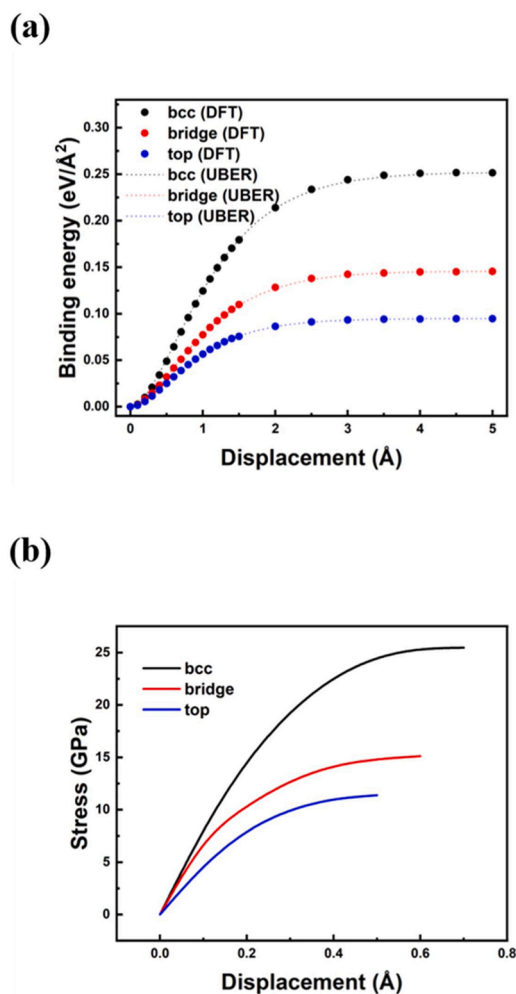
(a)

(b)

Fig. 4. (a) RGS tensile test for bcc-, bridge-, and top-type Fe(001)/Al(001) interface. The dotted line indicates the UBER fitting. (b) Strain-stress curve of bcc-, bridge-, and top-type Fe(001)/Al(001) interface as a function of displacement. The stress is obtained by the differentiating the UBER curves of (a).

energy–displacement curve as shown in Fig. 4(a), the theoretical–displacement relations of the Fe(001)/Al(001) interfaces could be obtained as shown in Fig. 4(b). The calculated tensile strengths of the bcc-, bridge-, and top-type Fe(001)/Al(001) interfaces were approximately 25.41, 15.10, and 11.37 GPa, respectively. Particularly, the bcc-type Fe(001)/Al(001) interface showed the highest tensile strength, which was also higher than that of the Al//IMCs and IMCs//IMCs interface structures [35,36], based on the RGS method.

3.3. Effect of oxidation

As discussed previously, in EMF, the jetting effect removes the oxide layer on the metal surface under specific collision conditions [22,23]. Further, the removal of the oxide layer is believed to substantially increase the bond strength. Therefore, it is necessary to determine the extent to which oxidation impacts the bond strength of the interface. This was investigated by inserting an oxygen atom at the bcc-type interface of Fe(001)/Al(001). Fig. 3(a) depicts the WS for the oxidized interface with different positions labeled 1 through 7. Position 4 corresponds to the interfaces of the Fe–O (oxidized model) or Fe–Al (bare model) atoms. The Al-O bond exhibited a stronger interaction than the Fe–O bond (Fig. S2 of Supporting Information). The WS of Fe–O, which was lower than that of Al–O, is shown in Fig. 5(a). Interestingly, the WS value decreased dramatically to ~0.067 eV/Å^2, which is considerably
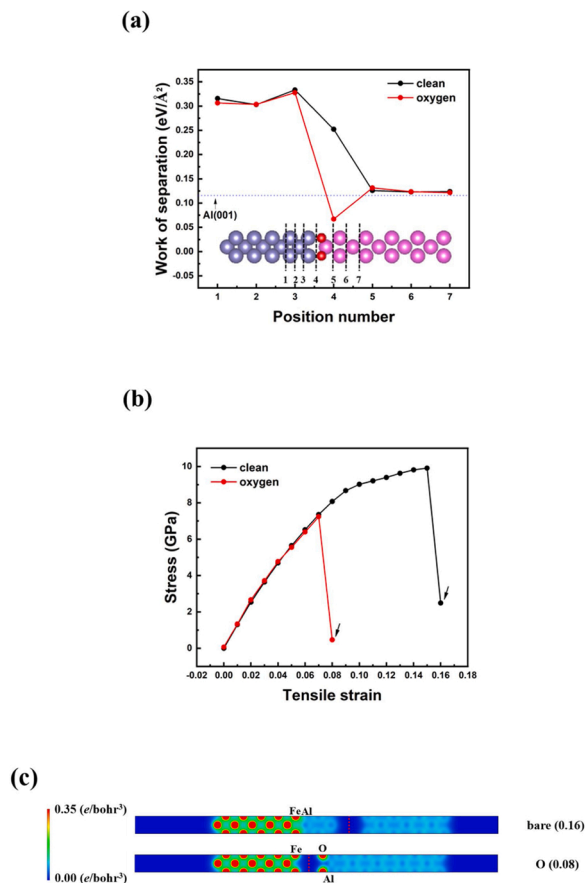
(a)

(b)

(c)

Fig. 5. (a) WS of the clean and oxidized bcc-Fe(001)/Al(001) interfaces with different positions. The insertion is the lateral view of the oxidized interface assigned with numbers. Herein, the red atom represents the oxygen atom. (b) Mechanical responses for clean and oxidized bcc interfaces. Mechanical deformation is applied along the [001] direction. (c) Charge distribution (in e/bohr^3) of the two models considered at the fracture strain, as indicated by the arrow in (b). In (c), the red dotted line indicates the failure region.

weaker than that of the pure Al(001) structure, due to the oxygen atom at the interface.

Additionally, we also confirmed that the presence of oxygen weakened the bond strength of the interface by observing the mechanical responses of the bare and oxidized bcc-type Fe(001)/Al(001) interface under tensile loading. Fig. 5(b) depicts the mechanical responses for the two models (with and without oxygen atoms) under the tensile strains in the thickness direction. Interestingly, both models exhibited similar stress-strain behaviors until the stress suddenly declined. A fracture occurred significantly earlier at the oxidized interface (tensile strain: ~0.08) than the clean interface (tensile strain: ~0.16). More importantly, the fracture initiated at the Al side of a clean interface, but occurred at the interface of the oxidized interface. This meant that the presence of oxygen at the interface severely weakened the bond strength. According to the Bader analysis (Fig. S2 in Supporting Information) of the oxidized interface, the O atom gained equal charge from the surrounding Fe and Al atoms, which was approximately 1.732e. Therefore, the O atom was ~0.866e from the Fe atom, which was less than that of the Fe–Al bond from the bcc and bridge interfaces. Consequently, the O atom hindered the interaction between the Fe and Al atoms at the interface. The charge distribution (in e/bohr^3) of the related models at the strain of the fracture is plotted in Fig. 5(c). Given the strong bond at the interface, the fracture was observed inside the Al part of the clean interface model, as shown in the upper part of Fig. 5(c). However, the O atom resulted in a fracture at the interface, as shown in the lower part of Fig. 5(c). These results implied that the jetting effect

should be large enough to remove the oxidation layer at the interface, to ensure strong welding between two dissimilar materials.

3.4. Effect of residual stress

Generally, the EMF process induces a high impulse to generate chemical or physical bonds between two dissimilar metals, which indicates that the mechanical stress is significantly applied to the structure during the process. Therefore, to understand the effect of the potential stress on the bond strength of the Fe(001)/Al(001) interface, we introduced biaxial loading (tension and compression) in directions parallel to the interface. Herein, 6 % biaxial compression and tension were applied to the interface structure, which is the strain before the initiation of the structural instability under lateral deformation to pure Al(001) and Fe (001) slabs. Fig. 6(a) shows the WS values at certain positions labeled in the inset of Fig. 5(a) under different loading conditions. Importantly, the WS at the interface remained almost the same, even when lateral deformation was applied. However, the matrix region of each Fe and Al part was moderately impacted, implying that the bond strength of the Fe (001)/Al(001) interface was not dependent on the in-plane deformation. In particular, the biaxial strains (compression and tension) caused a large change in the WS at the matrix region of Al, which was lower than that of the pure Al(001) slab. Subsequently, to compare the mechanical responses for the three different models, we additionally applied a tensile strain in the thickness direction, as shown in Fig. 6(b). The stiffness of the interface structure of the biaxial-stressed configurations was smaller than that of the free–strain along the thickness direction. Notably, owing to the mechanical deformation in the in-plane direction, the ideal strength of the interface structure decreased in the following order: biaxial compression (10.49 GPa), free-strain (9.91 GPa), and biaxial tension (9.53 GPa). This trend in the ideal strength was also observed in the bulk structure (not shown) under the same loading condition as the interface model. Fig. 6(c) shows the charge distribution of the Fe(001)/A(001) interface at the strain of the fracture under different loading conditions. In all the cases, the fracture initiated at the Al matrix region due to the similar or smaller WS as compared to the pure Al(001) slab, as shown in Fig. 6(a). Our results demonstrated that the residual stress induced during the EMF process could rarely impact the bond strength of the Fe(001)/Al(001) interface.

4. Conclusion

In summary, we performed first-principles calculations to observe the bond characteristics of the Fe(001)/Al(001) coherent interface. To achieve this, we considered the atomic configuration, oxidation at the interface, and application of the mechanical strain along the lateral direction. Initially, among the types of interfaces investigated, the bcc- and bridge-type interfaces exhibited higher strength than the pure Al(001) slab in terms of the WS, which could be employed to extract the interface fracture toughness and energy. Moreover, it indicated that the fracture could be initiated in the Al matrix. We confirmed that the bond strength was strongly related to the charge transfer between the Fe and Al atoms, as confirmed by the Bader analysis. The bcc interface showed the highest bond strength; nevertheless, the possibility of phase-transformation was predicted by the interfacial energy. Secondly, adding O atom between the Fe and Al atoms caused the bond strength to decrease significantly, to a value even smaller than that of pure Al(001). Given the weak interaction at the interface, the fracture occurred at the interface under 8 % strain along the thickness direction. However, the Al–Al bond of the clean bcc interface initially broke at a strain of 16 %. Our findings suggested that adequate jetting must be generated by controlling the welding conditions to obtain a strong bond at the interface. Lastly, the residual stress was confirmed by applying 6 % of the biaxial strain to the bcc interface structure along the lateral directions. We determined that the influence of lateral deformation on the bond strength at the interface was quite low. However, the WS at the Fe and Al matrix region changed
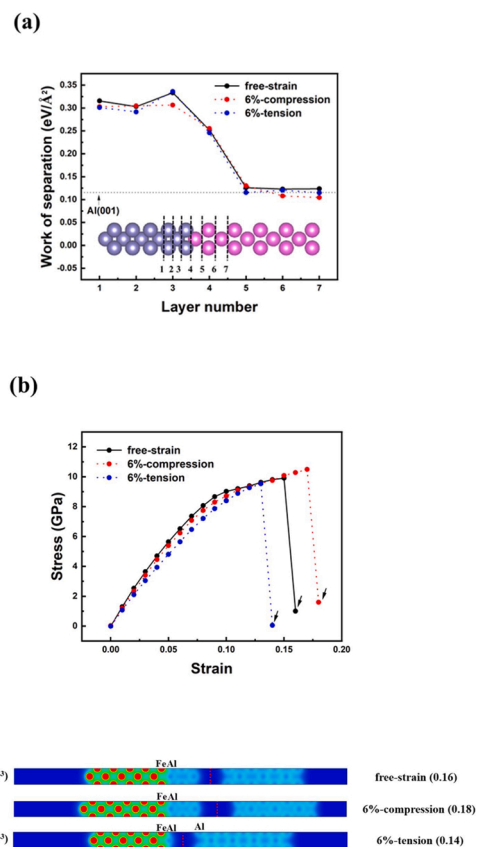

Fig. 6. (a) WS of the bcc Fe(001)/Al(001) interface under different loading conditions parallel to the interface direction. (b) Strain-stress curve for the three loading conditions. (c) Charge distribution (in e/bohr^3) of the fractured Fe (001)/Al(001) interface, indicated by the narrow in (b), with different loading conditions along the in-plane direction. In (c), the red dotted line indicates the failure region.

significantly upon applying lateral deformation to the structure, particularly in the fracture at the Al matrix, as the elongation increased along the thickness direction; that is there were no experimental restrictions that induced mechanical deformations under conditions in which the jetting effect could occur.

Declaration of Competing Interest

The authors declare that they have no known competing financial interests or personal relationships that could have appeared to influence the work reported in this paper.

Acknowledgements

Appendix A. Supplementary data

Supplementary material related to this article can be found, in the online version, at doi:https://doi.org/10.1016/j.mtcomm.2021.102107.

References

[1] B.L. Mordike, T. Ebert, Magnesium Properties - applications - potential, Mater. Sci. Eng. A 302 (2001) 37–45.

[2] M. Goede, M. Stehlin, L. Rafflenbeul, G. Kopp, E. Beeh, Super Light Car-lightweight construction thanks to a multi-material design and function integration, Eur. Transp. Res. Rev. 1 (2009) 5–10.

[3] G. Liedl, R. Bielak, J. Ivanova, N. Enzinger, G. Figner, J. Bruckner, H. Pasic, M. Pudar, S. Hampel, Joining of aluminum and steel in Car body manufacturing, Phys. Procedia 12 (2011) 150–156.

[4] W.J. Joost, Reducing vehicle weight and improving U.S. Energy efficiency using integrated computational materials engineering, JOM 64 (2012) 1032–1038.

[5] A. Buddery, M. Dargusch, D. StJohn, J. Drennan, S. Nabulsi, Laser welding of titanium and its alloys for medical applications: current knowledge and future direction, Mater. Sci. Forum 618–619 (2009) 291–294.

[6] G. Satoh, Y.L. Yao, C. Qiu, Strength and microstructure of laser fusion-welded Ti-SS dissimilar material pair, Int. J. Adv. Manuf. Technol. 66 (2013) 469–479.

[7] D. Burford, C. Widener, B. Tweedy, Advances in friction stir welding for aerospace applications, Airframer 4 (2006) 3–8.

[8] H.C. Chen, A.J. Pinkerton, L. Li, Fibre laser welding of dissimilar alloys of Ti-6Al-4V and Inconel 718 for aerospace applications, Int. J. Adv. Manuf. Technol. 52 (2011) 977–987.

[9] Y.C. Chen, K. Nakata, Microstructural characterization and mechanical properties in friction stir welding of aluminum and titanium dissimilar alloys, Mater. Des. 30 (2009) 469–474.

[10] Y. Chen, S. Chen, L. Li, Influence of interfacial reaction layer morphologies on crack initiation and propagation in Ti/Al joint by laser welding-brazing, Mater. Des. 31 (2010) 227–233.

[11] C. Yao, B. Xu, X. Zhang, J. Huang, J. Fu, Y. Wu, Interface microstructure and mechanical properties of laser welding copper-steel dissimilar joint, Opt. Lasers Eng. 47 (2009) 807–814.

[12] M. Weigl, M. Schmidt, Modulated laser spot welding of dissimilar copper-aluminium connections, Proceedings of 4 M/ICOMM Conference (2009) 211–214.

[13] Y.K. Kim, S.I. Hong, Effect of intermetallic compound layer on peel strength and crack propagation behavior in Cu/Al/Cu clad composites, Metals 9 (2019) 1155.

[14] J. Yan, Z. Xu, Z. Li, L. Li, S. Yang, Microstructure characteristics and performance of dissimilar welds between magnesium alloy and aluminum formed by friction stirring, Scripta Mater. 53 (2005) 585–589.

[15] C. Genevois, M. Girard, B. Huneau, X. Sauvage, G. Racineux, Interfacial reaction during friction stir welding of Al and Cu, Metall. Mater. Trans. A 42 (2011) 2290–2295.

[16] M.A. Mofid, E. Loryaei, Investigating microstructural evolution at the interface of friction stir weld and diffusion bond of Al and Mg alloys, J. Mater. Res. Technol. 8 (2019) 3872–3877.

[17] T. Löschmann, F. Putz, M. Koch, Perspektivische Genauigkeitsanforderungen im Automobilbau, Proceedings of ICAFT06 Conference (2006) 9–24.

[18] R. Schäfer, P. Pasquale, Electromagnetic pulse forming technology keys for allocating the industrial market segment, Proceedings of ICHSF Conference (2010) 16–25.

[19] G. Zittel, A historical review of high speed metal forming, Proceedings of ICHSF Conference (2010) 2–15.

[20] H. Daube, J. Götsch, A. Hänisch, Ausnutzung gespeicherter elektrischer Energie zur Magnetumformung von Metallen und Grenzen dieses Verfahrens, Fert. Und Betr. 16 (1966) 107–113.

[21] K. Faes, T. Baaten, W. De Waele, N. Debroux, Joining of copper to brass using magnetic pulse welding, Proceedings of ICHSF Conference (2010) 84–96.

[22] J.M. Walsh, R.G. Shreffler, F.J. Willig, Limiting conditions for jet formation in high velocity collisions, J. Appl. Phys. 24 (1953) 349–359.

[23] G.R. Cowan, A.H. Holtzman, Flow configurations in colliding plates: explosive bonding, J. Appl. Phys. 34 (1963) 928–939.

[24] A. Nassiri, A. Vivek, T. Abke, B. Liu, T. Lee, G. Daehn, Depiction of interfacial morphology in impact welded Ti/Cu bimetallic systems using smoothed particle hydrodynamics, Appl. Phys. Lett. 110 (2017), 231601.

[25] S.Y. Chen, Z.W. Wu, K.X. Liu, X.J. Li, N. Luo, G.X. Lu, Atomic diffusion behavior in Cu-Al explosive welding process, J. Appl. Phys. 113 (2013), 044901.

[26] J. Yang, J. Zhang, J. Qiao, Molecular dynamics simulations of atomic diffusion during the Al-Cu ultrasonic welding process, Materials 12 (2019) 2306.

[27] K. Czelej, K.J. Kurzydłowski, Ab initio prediction of strong interfacial bonding in the Fe|Al bimetallic composite system, Scr. Mater. 177 (2020) 162–165.

[28] M.Z. Khalid, J. Friis, P.H. Ninive, K. Marthinsen, A. Strandlie, A first-principles study of the Al (001)/Fe(0-11) interface, Mater. Sci. Forum 941 (2018) 2349–2355.

[29] G. Kresse, J. Furthmüller, Efficiency of ab-initio total energy calculations for metals and semiconductors using a plane-wave basis set, Comput. Mater. Sci. 6 (1996) 15–50.

[30] G. Kresse, J. Furthmüller, Efficient iterative schemes for ab initio total-energy calculations using a plane-wave basis set, Phys. Rev. B 54 (1996) 11169–11186.

[31] D. Joubert, From ultrasoft pseudopotentials to the projector augmented-wave method, Phys. Rev. B 59 (1999) 1758–1775.

[32] M. Perdew, J. P, K. Burke, Ernzerhof, Generalized gradient approximation made simple, Phys. Rev. Lett. 77 (1996) 3865–3868.

[33] H.J, P.J.D. Monkhorst, Special points for Brillouin-zone integrations, Phys. Rev. B 13 (1976) 5188.

[34] M. Yamaguchi, First-principles study on the grain boundary embrittlement of metals by solute segregation: part I. Iron (Fe)-solute (B, C, P, and S) systems, Metall. Mater. Trans. A 42 (2011) 319–329.

[35] M.Z. Khalid, J. Friis, P.H. Ninive, K. Marthinsen, A. Strandlie, Ab-initio study of atomic structure and mechanical behaviour of Al/Fe intermetallic interfaces, Comput. Mater. Sci. 174 (2020), 109481.

[36] M.Z. Khalid, J. Friis, P.H. Ninive, K. Marthinsen, A. Strandlie, First-principles study of tensile and shear strength of Fe-Al and α-AlFeSi intermetallic compound interfaces, Comput. Mater. Sci. 187 (2021), 110058.

[37] M. Černý, P. Šesták, P. Rehák, M. Všianská, M. Šob, Atomistic approaches to cleavage of interfaces, Model. Simul. Mater. Sci. Eng. 27 (2019).

[38] C. Qiu, Y. Su, B. Chen, J. Yang, Z. Li, Q. Ouyang, Q. Guo, D. Xiong, D. Zhang, First-principles investigation of interfacial stability, mechanical behavior and failure mechanism of β-SiC(1 1 1)/Al(1 1 1) interfaces, Comput. Mater. Sci. 175 (2020), 109608.

[39] D. Clatterbuck, The ideal strength of iron in tension and shear, Acta Mater. 51 (2003) 2271–2283.

[40] J. Yu, X. Lin, J. Wang, J. Chen, W. Huang, First-principles study of the relaxation and energy of bcc-Fe, fcc-Fe and AISI-304 stainless steel surfaces, Appl. Surf. Sci. 255 (2009) 9032–9039.

[41] J.A. Rayne, B.S. Chandrasekhar, Elastic constants of iron from 4.2 to 300°K, Phys. Rev. 122 (1961) 1714–1716.

[42] W.R. Tyson, W.A. Miller, Surface free energies of solid metals estimation from liquid surface tension measurements, Surf. Sci. 62 (1977) 267–276.

[43] N.E. Singh-Miller, N. Marzari, Surface energies, work functions, and surface relaxations of low-index metallic surfaces from first principles, Phys. Rev. B 80 (2009), 235407.

[44] D.M. Clatterbuck, C.R. Krenn, M.L. Cohen, J.W. Morris, Phonon instabilities and the ideal strength of aluminum, Phys. Rev. Lett. 91 (2003), 135501.

[45] G.N. Kamm, G.A. Alers, Low-temperature elastic moduli of aluminum, J. Appl. Phys. 35 (1964) 327–330.

[46] A.A. Griffith, The phenomena of rupture and flow in solids, Philos. Trans. R. Soc. London Ser. A 221 (1921) 163–198.

[47] V. Fiorentini, M. Methfessel, Extracting convergent surface energies from slab calculations, J. Phys. Condens. Matter 8 (1996) 6525–6529.

[48] Y. Han, D.J. Liu, Quantum size effects in metal nanofilms: Comparison of an electron-gas model and density functional theory calculations, Phys. Rev. B 80 (2009), 155404.

[49] Y. Han, K.C. Lai, A. Lii-Rosales, M.C. Tringides, J.W. Evans, P.A. Thiel, Surface energies, adhesion energies, and exfoliation energies relevant to copper-graphene and copper-graphite systems, Surf. Sci. 685 (2019) 48–58.

[50] K. Chen, M. Bielawski, Interfacial fracture toughness of transition metal nitrides, Surf. Coat. Technol. 203 (2008) 598–601.

[51] C. He, M. Cheng, M. Zhang, W.X. Zhang, Interfacial Stability and Electronic Properties of Ag/M (M = Ni, Cu, W, and Pd) and Cu/Cr Interfaces, J. Phys. Chem. C 122 (2018) 17928–17935.

[52] Y. Yuan, X. Gong, H. Wang, The synergistic mechanism of graphene and MoS₂ for hydrogen generation: Insights from density functional theory, Phys. Chem. Chem. Phys. 17 (2015) 11375–11381.

[53] C. He, J.H. Zhang, W.X. Zhang, T.T. Li, Type-II InSe/ g-C3N4 Heterostructure as a High-Efficiency Oxygen Evolution Reaction Catalyst for Photoelectrochemical Water Splitting, J. Phys. Chem. Lett. 10 (2019) 3122–3128.

[54] G. Henkelman, A. Arnaldsson, H. Jónsson, A fast and robust algorithm for Bader decomposition of charge density, Comput. Mater. Sci. 36 (2006) 354–360.

[55] R.S.E. Sanville, S.D. Kenny, Improved grid-based algorithm for bader charge allocation, J. Comput. Chem. 28 (2007) 899–908.

[56] W. Tang, E. Sanville, G. Henkelman, A grid-based Bader analysis algorithm without lattice bias, J. Phys. Condens. Matter 21 (2009), 084204.

[57] T. Li, C. He, W. Zhang, A novel porous C₄N₄ monolayer as a potential anchoring material for lithium-sulfur battery design, J. Mater. Chem. A 7 (2019) 4134–4144.

[58] T. Li, C. He, W. Zhang, Two-dimensional porous transition metal organic framework materials with strongly anchoring ability as lithium-sulfur cathode, Energy Storage Mater. 25 (2020) 866–875.

[59] R. Soulairol, C.C. Fu, C. Barreteau, Structure and magnetism of bulk Fe and Cr: from plane waves to LCAO methods, J. Phys. Condens. Matter 22 (2010), 295502.

[60] S. Lu, Q.M. Hu, M.P.J. Punkkinen, B. Johansson, L. Vitos, First-principles study of fcc-Ag/bcc-Fe interfaces, Phys. Rev. B 87 (2013), 224104.

[61] J.H. Rose, J. Ferrante, J.R. Smith, Universal binding energy curves for metals and bimetallic interfaces, Phys. Rev. Lett. 47 (1981) 675–678.

[62] R. Janisch, N. Ahmed, A. Hartmaier, Ab initio tensile tests of Al bulk crystals and grain boundaries: universality of mechanical behavior, Phys. Rev. B 81 (2010), 184108.

[63] P. Lazar, R. Podloucky, Cleavage fracture of a crystal: density functional theory calculations based on a model which includes structural relaxations, Phys. Rev. B 78 (2008), 104114.